*Key Engineering Materials*
*ISSN: 1662-9795, Vol. 1047, pp 333-345*

*Submitted: 2026-01-20*
*Accepted: 2026-02-11*
*Online: 2026-04-13*

# Effect of Preheating Temperature on the Optimal Processing Windows of Inconel 718 Processed by Laser Power Bed Fusion

Tchuindjang Jérôme Tchoufang[1,a*], Fassinato Edoardo[1,b], Dedry Olivier[1,c], Mertens Anne[1,d]

[1]Metallic Materials for Additive Manufacturing (MMS), Aerospace and Mechanical Engineering Dpt., Quartier POLYTECH 1, Allée de la Découverte 9 - 4000 Liège (Belgium)

[a*]J.Tchuindjang@uliege.be, [b]Edoardo.Fassinato@student.uliege.be, [c]Dedry.Olivier@uliege.be, [d]Anne.Mertens@uliege.be

**Keywords:** laser power bed fusion, inconel 718, preheating temperature, processing windows.

**Abstract.** Laser Powder Bed Fusion (LPBF) of Inconel 718 (IN718) enables near-net-shape fabrication of complex components but is limited by narrow processing windows, crack susceptibility, and defect formation. In this work, the influence of substrate preheating on LPBF processability, densification, microstructure, and hardness of IN718 is investigated. Cuboid samples ($10 \times 10 \times 10$ mm³) were fabricated at three preheating temperatures (80 °C, 300 °C, and 500 °C), while laser power was varied between 100 W and 200 W with fixed layer thickness (30 µm) and hatch spacing (80 µm). Density was assessed using helium pycnometry and optical microscopy, while both optical and scanning electron microscopy (SEM) were used to characterize melt pool (MP) geometry, cellular substructure, cracking behavior, and oxide inclusions. Vickers hardness (HV10) measurements were performed to assess as-built mechanical response under high load of 10kg, whereas micro hardness under a load of 0.3kg was used to evaluate the hardening and/or softening phenomena occurring during LPBF processing. The results show that increasing preheating temperature significantly widens the full-density processing window, suppresses cracking, stabilizes MPs, and promotes partial in-situ ageing, leading to enhanced as-built hardness. Nevertheless, to high preheating temperatures appear to promote both the occurrence of large porosities and the formation of oxides inclusions. These findings highlight the need for preheating-aware LPBF process metrics beyond classical volumetric energy density.

## Introduction

Inconel 718 (IN718) is a precipitation-strengthened Ni-based superalloy widely used in aerospace, power generation, and energy applications due to its excellent strength, creep resistance, and corrosion resistance up to approximately 650–700 °C [1–3]. Traditionally, IN718 components have been produced via casting or wrought thermomechanical processing routes, each optimized for specific performance and geometric requirements.

Casting enables the fabrication of large and complex geometries but is associated with dendritic segregation, Nb-rich interdendritic regions, and Laves phase formation, requiring extensive homogenization and solution-aging treatments [3,4]. Wrought processing, combined with standardized heat treatments such as AMS 5662, produces refined and homogeneous microstructures with superior fatigue and creep performance but offers limited geometric flexibility and incurs high manufacturing costs[3,5,6].

Additive manufacturing (AM) has emerged as a promising alternative, enabling design freedom, internal complexity, and part consolidation[7–9]. However, the unique thermal conditions of AM introduce new challenges related to defect formation, microstructural heterogeneity, and property control.

Among AM technologies, Powder Bed Fusion (PBF) and Directed Energy Deposition (DED) have been most widely investigated for IN718. DED processes offer high deposition rates and suitability for large components and repair applications but typically result in coarse MPs and limited geometric resolution[10–13]. Binder-based routes followed by sintering or hot isostatic pressing (HIP) have also been explored, although densification control and contamination sensitivity remain critical challenges[14].

Within PBF technologies, Laser Powder Bed Fusion (LPBF) and Electron Beam Melting (EBM) dominate. LPBF offers superior geometric resolution and fine solidification microstructures due to extremely high cooling rates [15,16]. However, LPBF of IN718 is constrained by steep thermal gradients, high residual stresses, and susceptibility to solidification and liquation cracking [17–19]. In contrast, EBM employs high powder-bed preheating temperatures that significantly reduce thermal gradients and residual stress, enabling crack-free builds and wider processing windows, albeit with coarser microstructures and lower surface resolution [20,21].

Achieving fully dense (>99.9%) LPBF IN718 components requires careful control of processing parameters to avoid multiple defect mechanisms. Most studies rely on processing maps involving laser power, scan speed, hatch spacing, and layer thickness, often condensed into the *volumetric energy density* (VED) as a first-order optimization metric [22–24].

At insufficient energy input, lack-of-fusion porosity dominates, whereas excessive energy densities promote keyhole-induced porosity and evaporation-related instabilities [25–27]. The acceptable processing window is further narrowed by solidification and liquation cracking, which are particularly severe in IN718 due to its solidification range and Nb segregation behavior [17–19]. Additional strategies such as scan-strategy optimization, contour passes, remelting, powder quality control, and atmosphere management have been shown to expand the density-safe window [28–31].

Despite its widespread use, VED has been increasingly recognized as an incomplete descriptor, as identical VED values may produce markedly different melt-pool geometries and defect populations depending on beam diameter, absorptivity, and thermal boundary conditions [32,33].

Recent studies have identified substrate and powder-bed preheating as a critical parameter governing LPBF processability of IN718 [34–38]. Preheating reduces heat extraction into the substrate, lowers thermal gradients, and decreases thermally induced tensile stresses, thereby significantly suppressing cracking. Elevated preheating temperatures also stabilize the MP and widen the full-density processing window [34,39,40]. Moreover, cumulative thermal exposure due to repeated layer reheating enables partial in-situ precipitation of γ″ and enhanced Nb back-diffusion, reducing microsegregation and Laves phase formation [41–44]. These benefits are accompanied by important trade-offs. Higher preheating temperatures increase oxidation kinetics and the likelihood of stable Al- and Si-rich oxide inclusions if oxygen control is insufficient [45–47]. Excessive thermal exposure may further promote δ-phase precipitation and microstructural coarsening, potentially impairing ductility and fatigue resistance [48,49].

A key gap in the literature lies in the lack of formal process metrics that incorporate preheating effects into LPBF optimization frameworks. Classical VED formulations neglect temperature-dependent sensible heat contributions and therefore fail to predict melting and stability thresholds across different preheating conditions [32,33]. Integrating preheating temperature into modified energy-based metrics and coupling these with effective ageing concepts derived from cyclic reheating provides a physically grounded framework linking energy input, melt-pool geometry, defect formation, in-situ precipitation, and mechanical properties. Such an approach enables transferable processing maps, rational comparison between LPBF and EBM, and predictive control of density and microstructure.

## Materials and Methods

### Material and LPBF processing conditions.

Gas-atomized Inconel 718 powder supplied by VDM Metals GmbH was used in this study. The powder exhibited a near-spherical morphology with a particle size distribution ranging from 15 to 52 μm, with D10, D50 and D90 values of 23 μm, 37 μm, and 55 μm respectively. Typical ranges for the average chemical composition include 50-55% Ni, 17-21% Cr, 4.75-5.5% Nb, 2.8-3.3% Mo, 0.6-1.15% Ti, 0.2-0.8% Al, with low C (<0.08%), S (<0.015%), and P (<0.015%).

All samples were manufactured using a Aconity mini LPBF system equipped with a continuous-wave fiber laser of 200W. Cuboid specimens with dimensions of 10 × 10 × 10 mm³ were fabricated on a 316L substrate under argon atmosphere. Three different substrate/powder-bed preheating

temperatures were investigated: 80 °C, 300 °C, and 500 °C. For each job, 20 cubes were printed based on various processing parameters.

The processing parameters were selected to explore the effect of energy input and preheating on density, defects, and microstructure. The laser power was varied between 100 W and 200 W, while the laser spot, the layer thickness and the hatching distance were kept constant at 80µm, 30 µm and 80 µm, respectively. The scan speed was adjusted accordingly between 200 mm/sec and 1000 mm/sec, to achieve a range of volumetric energy densities (VED), calculated as following Eq. (1):

$$\mathrm{VED} = \frac{P}{v \cdot h \cdot t} \quad (1)$$

Where ($P$) is the laser power, ($v$) the scan speed, ($h$) the hatch spacing, and ($t$) the layer thickness.

A bidirectional scanning strategy with 90° rotation between successive layers was employed for all builds to limit anisotropic heat accumulation.

**Density and porosity assessment.**

The density of the printed cubes was assessed using two complementary methods. Firstly, the Helium gas pycnometry provides bulk density values averaged from five measures over the entire specimen volume in g/cm³. And secondly , metallographic cross-section analysis was carried out, where samples were sectioned parallel to the build direction, mechanically ground, polished, and examined under an optical microscope. ImageJ analysis software was used to quantify porosity area fraction and pore morphology. The combined use of pycnometry and metallography allowed discrimination between closed porosity, open porosity, and crack-related defects.

**Microstructural characterization.**

Scanning Electron Microscopy (SEM) was employed to characterize microstructural features and defects. Backscattered electron (BSE) and secondary electron (SE) imaging modes were used to investigate cracks and non-metallic inclusions occurrence, cellular substructure and MP sizes. Energy Dispersive X-ray Spectroscopy (EDS) was used to identify the chemical nature of inclusions, with particular attention to Al-rich and Si-rich oxide particles.

**Hardness measurements.**

Vickers hardness measurements were performed on polished cross sections using a load of 10 kg (HV10) to assess bulk hardness, and a load of 0.3 kg for micro-hardness within the matrix. For each cube, a grid of 9 indentations (3 by 3 every 3 mm for HV 10, and 3 by 3 every 0.3 mm for HV0.3) was performed away from edges and visible defects. The reported hardness corresponds to the average value, with standard deviation used to assess property scatter.

## Results

**Density assessment, VED and Processing windows.**

Fig.1 give an overview of the printed cubes for the three preheating temperatures. Table 1 summarizes the values of the density as obtained from pycnometer measurements and the relative void area after optical microscope examination of cross sections. Only the samples considered as full dense are illustrated in Table 1 with their related VED values. Compared to pycnometry measurements, the results of quantitative metallography performed under optical microscopy always provide higher relative densities (Table 1). In addition, similar VED are found for samples printed under the same processing parameters, even when the preheating temperature is different (Table 1).

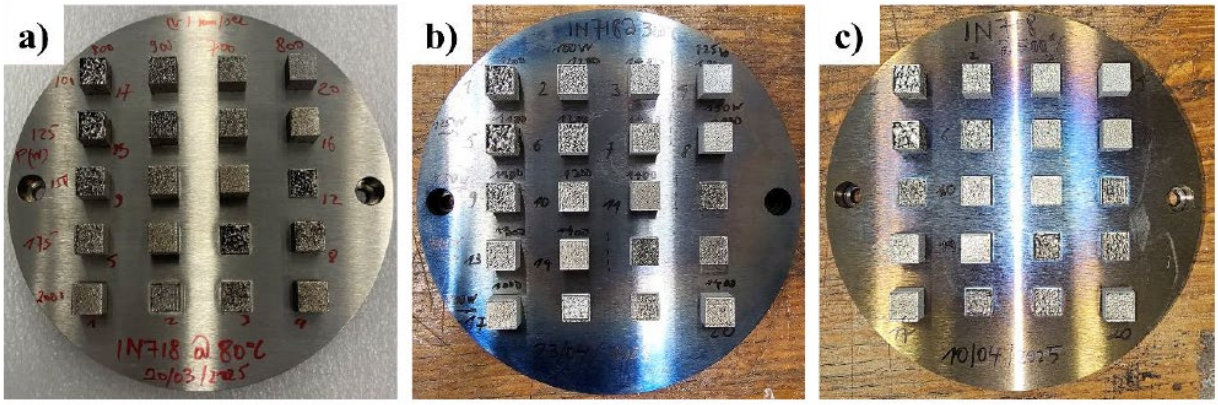


**Fig. 1.** Overview of as-built cuboid samples when considering preheating temperature of a) 80°C, b) 300°C and c) 500°C. The brownish contrast observed on both the substrate and the printed cubes at 500°C is the evidence of surface oxidation.

Fig.2 illustrates the various processing windows for each preheating temperature, as a function of laser power and scan speed. A narrow processing window was observed for all three preheating temperatures, where relative densities above 99,6% were achieved. This narrow processing window was set at 800 mm/sec for the scanning speed, while laser power varies between 150W and 200W for the preheating of 80°C, and between 100W and 200W for both 300°C and 500°C preheating temperatures. Increasing the preheating temperature from 80°C to 300°C and subsequently to 500°C resulted in a relative widening of the full-density processing window.

**Table 1.** Samples (cubes) with the processing parameters (*P* and *v*, assuming h and t to be constant) which exhibit relative density above 99.6%, and corresponding density (from pycnometer) and classical VED.

| Sample N° @T preheating | *P* (W) | *v* (mm/sec) | Density from pycnometer (g/cm³) | Relative density from OM (%) | VED (J/mm³) |
|---|---|---|---|---|---|
| 6@80°C | 150 | 800 | 8.22 | 99.70 | 78.13 |
| 1@80°C | 175 | 800 | 8.23 | 99.82 | 91.15 |
| 4@80°C | 200 | 800 | 8.21 | 99.65 | 104.17 |
| 8@300°C | 100 | 800 | 8.19 | 99.41 | 52.08 |
| 11@300°C | 125 | 800 | 8.21 | 99.62 | 65.10 |
| 14@300°C | 150 | 800 | 8.20 | 99.47 | 78.13 |
| 17@300°C | 175 | 800 | 8.19 | 99.43 | 91.15 |
| 20@300°C | 200 | 800 | 8.21 | 99.59 | 104.17 |
| 8@500°C | 125 | 800 | 8.24 | 99.66 | 65.10 |
| 11@500°C | 150 | 800 | 8.21 | 99.67 | 78.13 |
| 14@500°C | 175 | 800 | 8.22 | 99.88 | 91.15 |
| 20@500°C | 200 | 800 | 8.22 | 99.62 | 104.17 |

At the highest preheating temperature (500 °C), the processing window further widened. Full-density cubes were obtained over a broad VED range, with pycnometry measurements consistently exceeding 99.95%. Optical cross sections revealed a near-complete suppression of lack-of-fusion defects and a strong reduction in crack density.

**Porosity characteristics.**

Optical microscopy revealed that porosity morphology strongly depends on both VED and preheating temperature. At low preheating, pores were predominantly irregular and elongated, characteristic of lack-of-fusion defects. At high VED values, near-spherical pores consistent with keyhole porosity were observed (Fig. 3).

With increasing preheating temperature, the overall porosity fraction decreased, and pores became fewer and more uniformly distributed. At 500 °C preheating, porosity was mostly limited to isolated spherical pores, but their size significantly increased (Fig.3).

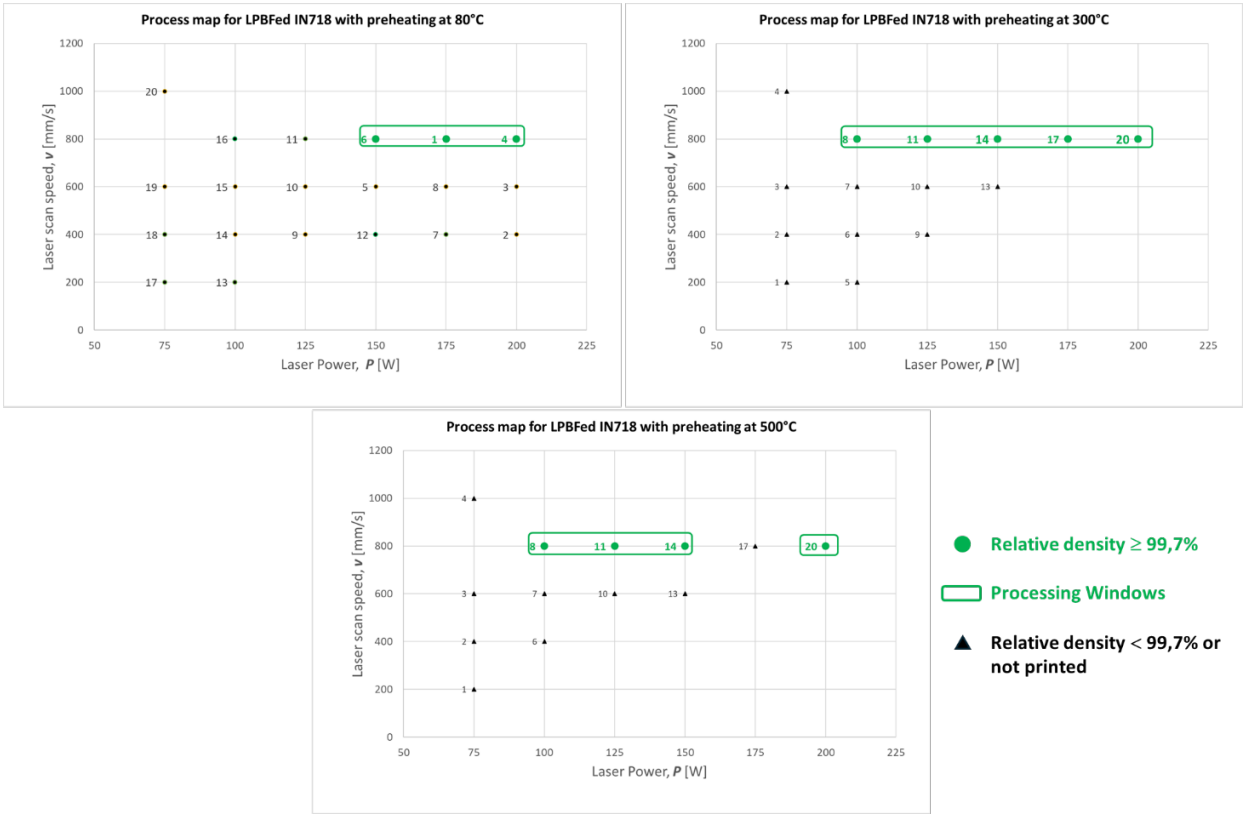


**Fig. 2.** Processing maps for Inconel 718 cuboid samples printed using LPBF process and preheating temperature of 80C, 300°C and 500°C, with evidence of a single scan speed of 800 mm/sec allowing full-dense specimens (more than 99,7%, as determined by pycnometer).

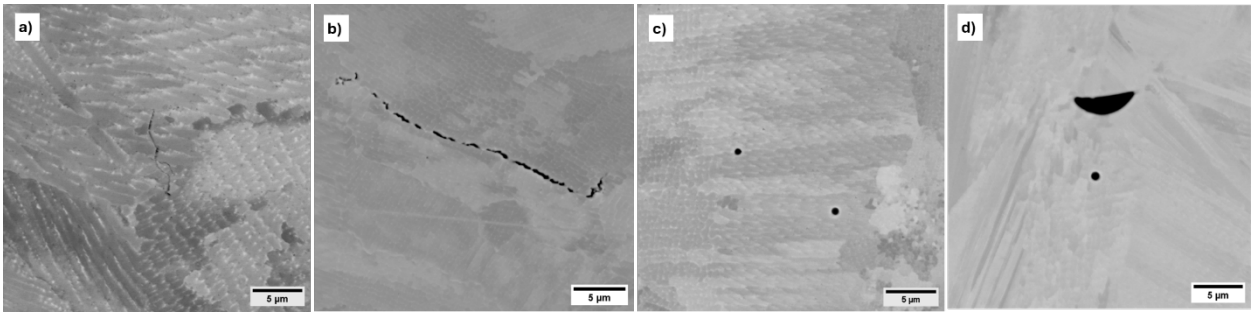


**Fig. 3.** Various micrographs as observed from SEM after Aqua regia etching showing cellular-like structure within the matrix and : a) solidification crack in sample 4@80°C; b) Si-rich oxide inclusion stringer at grain boundary in sample 4@80°C; c) middle-sized porosities entrapped in the matrix; and d) oversized inclusion and middle-sized porosity in sample 14@500°C.

**Cracking and inclusion behavior.**

Crack was frequently observed in samples printed at 80°C preheating. Such defects that are ascribed to solidification cracks propagated preferentially along MP and grain boundaries (Fig.3), which is consistent with solidification and liquation cracking mechanisms [50,51].

At both 300°C and 500°C preheating, cracking was significantly reduced and limited to isolated regions, indicating that thermal stress levels were below the critical cracking threshold.

SEM-EDS analysis allows identifying non-metallic inclusions that were primarily made of Al-rich and Si-rich oxides (Fig.4). The frequency of these inclusions increased slightly with preheating temperature, suggesting enhanced oxidation kinetics at elevated temperatures. These inclusions were

typically located at MP boundaries or entrapped within solidified tracks. The origin of oxygen was assumed to be the environment within the chamber, even if the content is around few ppm due to argon flux. Nevertheless, it has been observed during LPBF processing that powder change its color to a brownish one, which suggests that some oxide layer form within the surface of the powder prior to 3D printing. Such a phenomenon has already been highlighted by Beyhaghi and co-workers [46] who highlighted that residual oxygen present within the environment was initially released inside the melt. Then after the retained gas can either agglomerate to form a pore that is entrapped during solidification, or else it can be fixed by both Si and Al which segregated to grain boundaries at the end of the solidification and thus form non-metallic oxide inclusions subsequently.

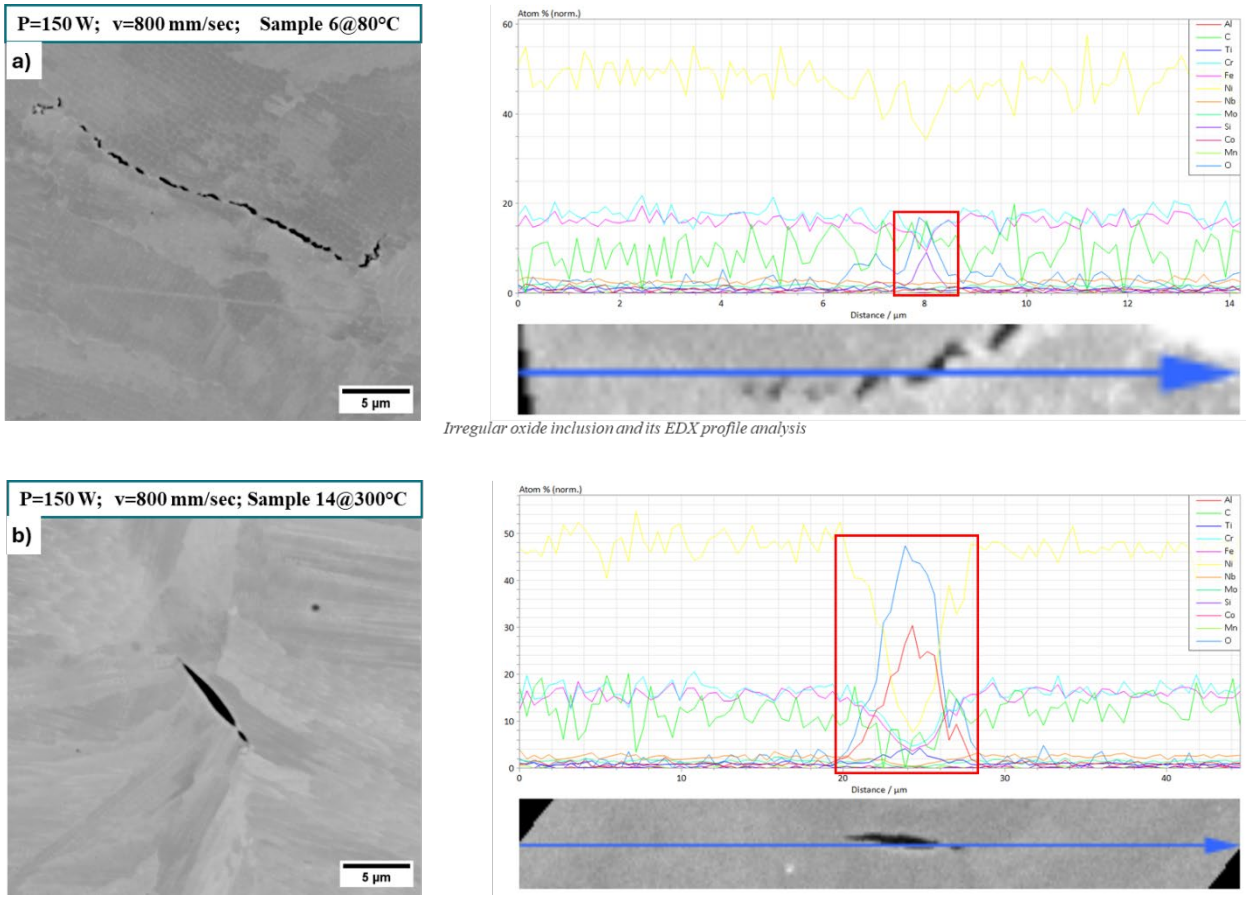


*Irregular oxide inclusion and its EDX profile analysis*

**Fig. 4.** EDS profiles performed on oxide inclusions at grain boundaries with cellular-like structure for which variations within the elements content can be linked to micro-segregations at cell-boundaries; a) Si rich oxide stringer in sample 6@80°C; b) mixed Al-rich and Si-rich elongated oxide inclusion in sample 14@300°C.

**Hardness evolution and as-built strengthening behavior.**

From the previous optical characterization, the following samples exhibiting more than 99,7% relative density were considered for hardness measurements: samples 4 and 6 @80°C, samples 14 and 17 @300°C, and samples 14 and 20 @500°C. All the retained samples were printed at v = 800 mm/sec. The related P for each sample is illustrated in Table 1. The hardness results are given within Fig.5 below. The average Vickers hardness exhibited a clear dependence on preheating temperature. Samples printed at 80°C showed moderate macro hardness values, primarily attributed to fine cellular substructures and residual stresses.

At 300°C preheating, the macro hardness decreases slightly despite some coarsening of the cellular structure. This increase can be related to partial stress relaxation combined with reduced defect content. The macro hardness looks like that of 300°C when the preheating temperature increases to 500°C

The trend is different when considering micro hardness, as there is a U-shape with higher hardness at 80°C followed by a hardness collapse at 300°C before a significant increase to maximum values for 500°C. This behavior is consistent with the onset of in-situ ageing, where repeated thermal cycling during the building promotes partial γ″ precipitation.
Hardness results demonstrate that preheating not only influences defect suppression but also directly affects strengthening and softening mechanisms in the as-built condition.

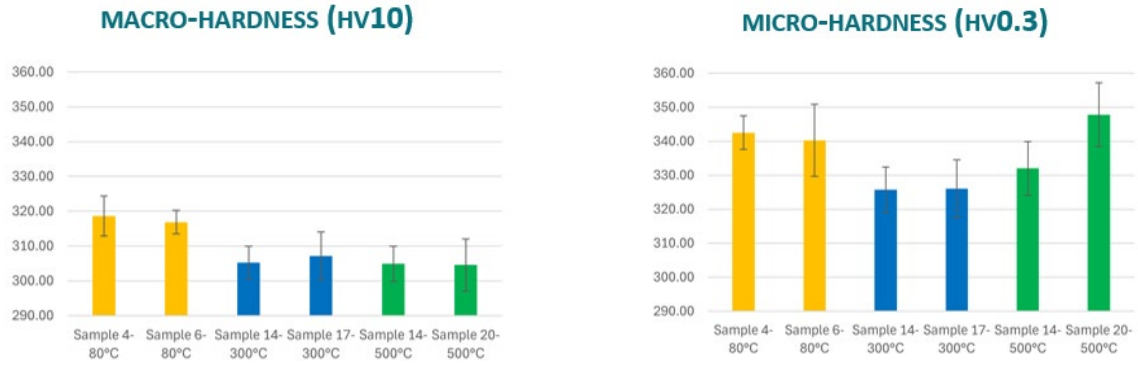


**Fig. 5.** Overview of hardness as obtained on the full-dense cubes after printing at various preheating temperatures that shows a decreasing trend for the macro hardness with increasing preheating temperature, and a U-shape trend for micro hardness; a) Macro hardness at 10 kg; b) micro hardness at 0.3 kg.

**Melt pool geometry/size and cellular substructure.**

Light microscope analysis showed that MP dimensions increased moderately with increasing preheating temperature at comparable VED values. The sizes that have been measured encompassed the average depth (*d*) on the top layer for both samples 14@300°C and 14@500°C, and average curvature radius (*R*)close to the top layer for the two previous samples and sample 6@80°C (Fig.6 and Table 2). The MP looks shallower for the highest preheating temperature of 500°C compared to that of 300°C. Nevertheless, the apparent MP width increase with the preheating temperature, based on the radius curvature that was measured on the bottom on the MPs. At 80 °C, MPs were narrow and deep, indicative of steep thermal gradients. Conversely, at 300°C and 500°C, MPs became wider and more stable, consistent with reduced heat extraction into the substrate.

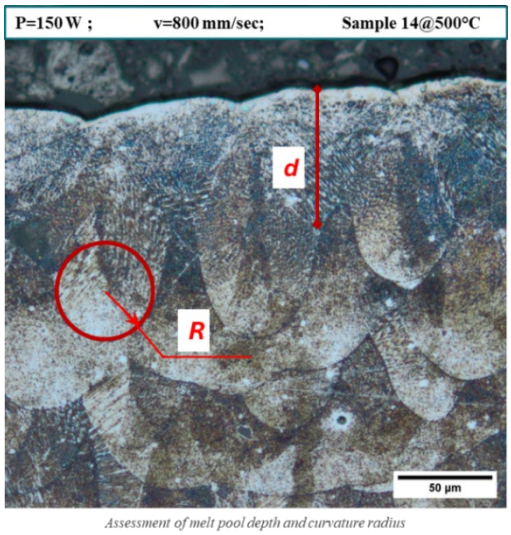


**Fig. 6.** Overview of the method used to assess both *d,* the depth of the MP (on the top layer), and the average curvature radius R.

**Table 2.** Results of the measurements of d and R on three samples printed with similar P and v, but different preheating temperature.

| Samples | Average MP depth, d (µm) | Average curvature radius, R (µm) |
|---|---|---|
| 6@80°C | - | 22.1±3.6 |
| 14@300°C | 70.1±17.0 | 24.0±2.6 |
| 14@500°C | 67.1±8.5 | 26.7±3.6 |

## Discussion

### Influence of preheating on LPBF processing windows and densification.

The results clearly demonstrate that preheating temperature is a first-order parameter controlling LPBF processability of Inconel 718. At 80°C preheating, the full-density processing window is narrow and highly sensitive to laser power and scan speed. Increasing the preheating temperature to 300°C significantly widens the density-safe window. These results highlight that preheating reduces both thermal gradients and cooling rates, stabilizing conduction-mode melting and making the process more robust to parameter fluctuations. Importantly, this widening of the process window cannot be captured by classical VED alone, underscoring the need for preheating-aware process metrics. Fully dense cubes are obtained over a broad VED range, and cracking is almost completely suppressed. Nevertheless, higher preheating temperatures seem to promote both numerous oxides inclusions and large pores formation.

### Limitation of the classical VED and approaches to consider preheating temperature.

The standard Eq. (1) used for VED implicitly assumes that the powder and substrate start at a constant initial temperature (typically near room temperature), and that melting is driven solely by laser energy. However, preheating reduces the sensible heat required to raise the material from the base temperature to the melting temperature. A physically consistent correction is to normalize VED by the temperature-dependent melt enthalpy. A simplified expression for the energy required to reach melting is given by Eq. (2):

$$E_{\text{melt}}(T) \approx \rho\, c_p\, (T_m - T) \tag{2}$$

Where typical IN718 values are $\rho = 8.19 \times 10^{-3}\text{g·mm}^{-3}$, $c_p = 0.435\text{J·g}^{-1}\text{·K}^{-1}$ and $T_m \approx 1350°\text{C}$
An equivalent VED hereinafter referred to as VED* can thus be set as in the following Eq. (3):

$$\text{VED}^*(T) = \text{VED} \times \frac{E_{\text{melt}}(T_0)}{E_{\text{melt}}(T)} \tag{3}$$

with $T_0 = 25°\text{C}$ as a reference temperature.
Another way to adapt VED while considering preheating temperature that is more rigorous, can be a thermodynamic-based approach. In this case, the laser energy density is compared with the actual energy required to melt the material volume, accounting for preheating:

$$E_{\text{fusion}} = \rho\left[c_p(T_m - T_{\text{preheat}}) + L_f\right] \tag{4}$$

Where $T_m$is the melting temperature and $L_f$is the latent heat of fusion. A dimensionless energy ratio can then be defined as follows:

$$\eta_E = \frac{\text{VED}}{E_{\text{fusion}}} \tag{5}$$

This ratio is more meaningful when comparing different preheating temperatures, different materials, or different processes (LPBF vs EBM).
From the previous Eq. (2) and (3), the following Table 3 is illustrated that compared classical VED with modified VED*. It appears that VED* increases with preheating temperature, following a trend like the one observed within the curvature radius of the MP. Therefore, it might be possible to further draw a relevant correlation that helps to predict MP size and shape from VED*, given the fact that energy absorption is considered. In addition, it has been well established that the depth and the width of the MP will vary with preheating temperature, but not in the same trend, due to melting modes or regimes [52–54]. The depth of the MP will increase monotonically with preheating temperature regardless of the conduction, transition or keyhole regime, whereas for the MP width, variations will depend on the melting regime.

**Cracking suppression through thermal gradient control.**

Cracking behavior exhibits a strong dependence on preheating temperature. At 80°C, cracks are frequently observed along MP and grain boundaries, consistent with solidification and liquation cracking driven by high thermal stresses. At 300°C, cracking is quite fully eliminated, the same result being more significantly achieved at 500°C. This suggest that thermal stresses fall below the critical threshold for crack initiation. This behavior parallels that reported for EBM, suggesting that sufficiently high preheating enables LPBF to emulate EBM-like thermal conditions while retaining the geometric resolution of laser-based processing.

**Table 3.** Classical VED calculated for various laser power values applied during LPBF processing on IN 718 (100W to 200W), while assuming other parameters to be constant (v = 800 mm/sec, t = 30µm and h = 80 µm) and comparison with equivalent VED* that takes into account the preheating temperature of the substrate set at 80°C, 200°C, 300°C and 500°C).

| Power (W) | VED (J/mm³) | VED* @ 80 °C | VED* @ 200 °C | VED* @ 300 °C | VED* @ 500 °C |
|---|---|---|---|---|---|
| 100 | 52.1 | 54.3 | 60.0 | 65.7 | 81.2 |
| 125 | 65.1 | 67.9 | 75.0 | 82.2 | 101.5 |
| 150 | 78.1 | 81.5 | 90.0 | 98.6 | 121.8 |
| 175 | 91.1 | 95.1 | 105.0 | 115.0 | 142.1 |
| 200 | 104.2 | 108.7 | 120.0 | 131.4 | 162.4 |

**Oxide inclusions and environmental sensitivity.**

SEM-EDS analysis confirms the presence of Si-rich oxide inclusions in all samples, with a slightly higher frequency at elevated preheating temperatures. Si-rich inclusions are distributed as stringers that often set the origin of cracks within samples preheated at 80°C. Conversely, both Si-rich and Al-rich oxides inclusions are present when higher preheating temperatures are considered, such as 300°C and 500°C. The size of Si-rich inclusions increases within these samples compared to 80°C, whereas needle-like Al-rich appear larger than Si-rich inclusions. Increasing the preheating temperature allow forming Al-rich inclusions. This observation highlights a critical trade-off. High preheating temperatures increase both the thermodynamic driving force and kinetic likelihood of oxide formation, especially when oxygen is introduced via powder surface contamination, powder reuse, or residual oxygen in the processing atmosphere. Si-rich oxides that preferentially form due to the high oxygen affinity of silicon, often appear as amorphous or glassy inclusions that act as crack initiation sites. Al-rich oxides are thermodynamically stable, hard, and brittle, and may survive repeated melting cycles as persistent inclusions.

As a result, high-preheat processing windows require stringent control of oxygen partial pressure and powder chemistry to avoid inclusion-related degradation of fatigue and fracture performance.

These inclusions, often trapped at MP boundaries, may act as preferential sites for fatigue crack initiation.

**Hardness evolution: in-situ hardening versus softening mechanisms.**

Vickers hardness measurements reveal a non-monotonic dependence on preheating temperature. Macro hardness collapses when preheating temperature increases, and the minimum of 305 HV10 that is almost reached at 300°C remain similar at 500°C. Conversely, there is a decreasing trend for micro hardness when increasing preheating temperature from 80°C 343 HV0.3) to 300°C (325 HV0.3), prior to a significant increase of the micro hardness up to the maximum of 346 HV0.3 achieved at 500°C. It can therefore be assumed that at macro scale, when considering several grains, the bulk hardness is driven both by the cellular structures and the residual stresses. Conversely, the micro-hardness may be more affected by both precipitates and dislocations as the depth of the indent is small [55]. Micro hardness is also reported to be more influence by local work hardening, the location according to the building direction, and the anisotropy [56]. Therefore, the decrease observed within the macro hardness when increasing preheating temperature in the as-built conditions should be ascribed

to partial to complete stress relaxation. At the micro scale that corresponds to the cellular matrix, the decrease within the micro hardness to a minimum reached at 300°C, prior to a steep increase at 500°C preheating temperature suggest the onset of in-situ ageing between 300°C and 500°C. Repeated thermal cycling at elevated base temperatures promotes partial γ″ precipitation, contributing to precipitation hardening in the as-built condition. However, hardness saturation and occasional local softening suggest competing effects from cell coarsening or early-stage over-ageing. These results demonstrate that preheating directly influences both strengthening and softening mechanisms.

## Conclusion

It is possible to process IN718 alloy under LPBF with preheating temperature of the stage to achieve full dense specimens. For given processing parameters, the soundness of the specimens depends upon the preheating temperature.

Preheating temperature is a first-order parameter controlling LPBF processability of Inconel 718. Preheating reduces thermal gradients and suppresses cracking, thereby widening the full-density processing window beyond what can be achieved by laser parameter optimization alone. But too high preheating temperatures yield oxidation of the powder feedstock and subsequently, large oxide inclusions will be formed at the end of the solidification of the material, together with gas that will be entrapped, leading to large pores in the as-built conditions.

VED alone is not enough to predict the quality of the printed samples. Therefore, an equivalent feature that considers the preheating temperature has been set as VED*, which can be useful to predict MP size.

## References

[1] Satyanarayana, D. V. V., and Eswara Prasad, N. “Nickel-Based Superalloys.” In: Prasad, N. E., Wanhill, R. J. H., eds. Aerospace Materials and Material Technologies : Volume 1: Aerospace Materials. Singapore, Springer, 2017. pp. 199–228.

[2] Bian, Z., Li, M., Liu, H., et al. “Comprehensive Optimization of Tensile and Creep Properties of Inconel 718 Superalloy at Room Temperature and Elevated Temperature Through Grain Boundary Engineering Treatments,” 2024.

[3] Bryndza, G., Tchuindjang, J. T., Chen, F., et al. “Review of the Microstructural Impact on Creep Mechanisms and Performance for Laser Powder Bed Fusion Inconel 718,” *Materials*, V. 18, No. 2, 2025, p. 276.

[4] Darolia, R. “Development of strong, oxidation and corrosion resistant nickel-based superalloys: critical review of challenges, progress and prospects,” *International Materials Reviews*, V. 64, No. 6, 2019, pp. 355–80.

[5] Radavich, J. F., and Carneiro, T. “A microstructural study of alloy 718 Plus,” *Superalloys*, V. 718, 2005, pp. 625–706.

[6] Ajay, P., and Dabhade, V. V. “Heat treatments of Inconel 718 nickel-based superalloy: A Review,” *Metals and Materials International*, V. 31, No. 5, 2025, pp. 1204–31.

[7] Yang, S., Tang, Y., and Zhao, Y. F. “A new part consolidation method to embrace the design freedom of additive manufacturing,” *Journal of Manufacturing Processes*, V. 20, 2015, pp. 444–9.

[8] DebRoy, T., Wei, H. L., Zuback, J. S., et al. “Additive manufacturing of metallic components – Process, structure and properties,” *Progress in Materials Science*, V. 92, 2018, pp. 112–224.

[9] Schmelzle, J., Kline, E. V., Dickman, C. J., et al. “(Re)Designing for Part Consolidation: Understanding the Challenges of Metal Additive Manufacturing,” *Journal of Mechanical Design*, V. 137, No. 111404, 2015.

[10] Liu, M., Kumar, A., Bukkapatnam, S., et al. “A review of the anomalies in directed energy deposition (DED) processes & potential solutions-part quality & defects,” *Procedia Manufacturing*, V. 53, 2021, pp. 507–18.

[11] Herzog, D., Seyda, V., Wycisk, E., et al. “Additive manufacturing of metals,” *Acta Materialia*, V. 117, 2016, pp. 371–92.

[12] Saboori, A., Aversa, A., Marchese, G., et al. “Application of directed energy deposition-based additive manufacturing in repair,” *Applied Sciences*, V. 9, No. 16, 2019, p. 3316.

[13] Lehmann, T., Rose, D., Ranjbar, E., et al. “Large-scale metal additive manufacturing: a holistic review of the state of the art and challenges,” *International Materials Reviews*, V. 67, No. 4, 2022, pp. 410–59.

[14] Li, M., Du, W., Elwany, A., et al. “Metal Binder Jetting Additive Manufacturing: A Literature Review,” *Journal of Manufacturing Science and Engineering*, V. 142, No. 090801, 2020.

[15] Jiang, C.-P., Masrurotin., Wibisono, A. T., et al. “Enhancing internal cooling channel design in Inconel 718 turbine blades via laser powder bed fusion: a comprehensive review of surface topography enhancements,” *International Journal of Precision Engineering and Manufacturing*, V. 26, No. 2, 2025, pp. 487–511.

[16] Cobbinah, P. V., Nzeukou, R. A., Onawale, O. T., et al. “Laser powder bed fusion of potential superalloys: a review,” *Metals*, V. 11, No. 1, 2020, p. 58.

[17] Wu, H., Zhou, J., Huang, L., et al. “Advances in Crack Formation Mechanisms, Evaluation Models, and Compositional Strategies for Additively Manufactured Nickel-Based Superalloys,” *Computer Modeling in Engineering & Sciences*, V. 143, No. 3, 2025, p. 2675.

[18] Jeong, S. G., Ahn, S. Y., Kim, E. S., et al. “Liquation cracking in laser powder bed fusion-fabricated Inconel718 of as-built, stress-relieved, and hot isostatic pressed conditions,” *Materials Science and Engineering: A*, V. 888, 2023, p. 145797.

[19] Zhang, Y., Yang, L., Chen, T., et al. “Sensitivity of liquation cracking to deposition parameters and residual stresses in laser deposited IN718 alloy,” *Journal of Materials Engineering and performance*, V. 26, No. 11, 2017, pp. 5519–29.

[20] Li, Y., Long, H., Wang, Y., et al. “A novel and high-efficiency dual-electron gun concurrent preheating additive manufacturing technology: suppressing thermal cracks in non-weldable IN738LC nickel-based superalloy by mitigating temperature fluctuations,” *Virtual and Physical Prototyping*, V. 20, No. 1, 2025, p. e2518615.

[21] Fu, Z., and Körner, C. “Actual state-of-the-art of electron beam powder bed fusion,” *European Journal of Materials*, V. 2, No. 1, 2022, pp. 54–116.

[22] Yue, T., Zou, Z., Zhang, S., et al. “Effects of volumetric energy density on melting modes, printability, microstructures, and mechanical properties of laser powder bed fusion (L-PBF) printed pure nickel,” *Materials Science and Engineering: A*, V. 909, 2024, p. 146871.

[23] Pramod, S., and Kesavan, D. “Melting modes of laser powder bed fusion (L-PBF) processed IN718 alloy: Prediction and experimental analysis,” *Advances in Industrial and Manufacturing Engineering*, V. 6, 2023, p. 100106.

[24] Hu, Y., Jia, H.-B., Hu, Y.-Q., et al. “Thermal cycling on microstructure and mechanical properties of laser powder bed fusion manufactured IN738LC alloy,” *Rare Metals*, V. 43, No. 12, 2024, pp. 6649–72.

[25] Haribaskar, R., and Kumar, T. S. “Defects in metal additive manufacturing: formation, process parameters, postprocessing, challenges, economic aspects, and future research directions,” *3D Printing and Additive Manufacturing*, V. 11, No. 4, 2024, pp. e1629–55.

[26] Guo, L., Liu, H., Wang, H., et al. “Identifying the keyhole stability and pore formation mechanisms in laser powder bed fusion additive manufacturing,” *Journal of Materials Processing Technology*, V. 321, 2023, p. 118153.

[27] Huang, Y., Fleming, T. G., Clark, S. J., et al. “Keyhole fluctuation and pore formation mechanisms during laser powder bed fusion additive manufacturing,” *Nature communications*, V. 13, No. 1, 2022, p. 1170.

[28] Pant, P., Salvemini, F., Proper, S., et al. “A study of the influence of novel scan strategies on residual stress and microstructure of L-shaped LPBF IN718 samples,” *Materials & design*, V. 214, 2022, p. 110386.

[29] Liu, L., Wang, D., Yang, Y., et al. “Effect of scanning strategies on the microstructure and mechanical properties of inconel 718 alloy fabricated by laser powder bed fusion,” *Advanced Engineering Materials*, V. 25, No. 5, 2023, p. 2200492.

[30] Gruber, K., Smolina, I., Kasprowicz, M., et al. “Evaluation of Inconel 718 metallic powder to optimize the reuse of powder and to improve the performance and sustainability of the laser powder bed fusion (LPBF) process,” *Materials*, V. 14, No. 6, 2021, p. 1538.

[31] Newell, D. J., O’Hara, R. P., Cobb, G. R., et al. “Mitigation of scan strategy effects and material anisotropy through supersolvus annealing in LPBF IN718,” *Materials Science and Engineering: A*, V. 764, 2019, p. 138230.

[32] Caiazzo, F., Alfieri, V., and Casalino, G. “On the relevance of volumetric energy density in the investigation of Inconel 718 laser powder bed fusion,” *Materials*, V. 13, No. 3, 2020, p. 538.

[33] de Leon Nope, G. V., Perez-Andrade, L. I., Corona-Castuera, J., et al. “Study of volumetric energy density limitations on the IN718 mesostructure and microstructure in laser powder bed fusion process,” *Journal of Manufacturing Processes*, V. 64, 2021, pp. 1261–72.

[34] Kakehi, K., Chowdhury, H. T., Shinoda, Y., et al. “Effects of base plate temperature on microstructure evolution and high-temperature mechanical properties of IN718 processed by laser powder bed fusion using simulation and experiment,” *The International Journal of Advanced Manufacturing Technology*, V. 130, No. 11, 2024, pp. 5777–93.

[35] Shrivastava, A., Kumar, S. A., Rao, S., et al. “Exploring How LPBF process parameters impact the interface characteristics of LPBF Inconel 718 deposited on Inconel 718 wrought substrates,” *Optics & Laser Technology*, V. 174, 2024, p. 110571.

[36] Ur Rehman, A., Pitir, F., and Salamci, M. U. “Laser powder bed fusion (LPBF) of In718 and the impact of pre-heating at 500 and 1000° C: Operando Study,” *Materials*, V. 14, No. 21, 2021, p. 6683.

[37] Baldi, N., Giorgetti, A., Palladino, M., et al. “Study on the Effect of Preheating Temperatures on Melt Pool Stability in Inconel 718 Components Processed by Laser Powder Bed Fusion,” *Metals*, V. 13, No. 10, 2023, p. 1792.

[38] Zielinski, J., Theunissen, J., Kruse, H., et al. “Understanding Inhomogeneous Mechanical Properties in PBF-LB/M Manufactured Parts Due to Inhomogeneous Macro Temperature Profiles Based on Process-Inherent Preheating,” *Journal of Manufacturing and Materials Processing*, V. 7, No. 3, 2023, p. 88.

[39] Chen, Y., Wang, W., Ou, Y., et al. “Effect of high preheating on the microstructure and mechanical properties of high gamma prime Ni-based superalloy manufactured by laser powder bed fusion,” *Journal of Alloys and Compounds*, V. 960, 2023, p. 170598.

[40] Ur Rehman, A., Pitir, F., and Salamci, M. U. “Laser Powder Bed Fusion (LPBF) of In718 and the Impact of Pre-Heating at 500 and 1000 °C: Operando Study,” *Materials*, V. 14, No. 21, 2021, p. 6683.

[41] Wang, X., and Chou, K. “Effects of thermal cycles on the microstructure evolution of Inconel 718 during selective laser melting process,” *Additive Manufacturing*, V. 18, 2017, pp. 1–14.

[42] Zhang, H., Wu, Y., Wang, Y., et al. “In-situ nanoscale precipitation behavior and strengthening mechanism of WC/IN718 composites manufactured by laser powder bed fusion,” *Composites Part B: Engineering*, V. 284, 2024, p. 111727.

[43] Tucho, W. M., Cuvillier, P., Sjolyst-Kverneland, A., et al. “Microstructure and hardness studies of Inconel 718 manufactured by selective laser melting before and after solution heat treatment,” *Materials Science and Engineering: A*, V. 689, 2017, pp. 220–32.

[44] Kumara, C., Balachandramurthi, A. R., Goel, S., et al. “Toward a better understanding of phase transformations in additive manufacturing of Alloy 718,” *Materialia*, V. 13, 2020, p. 100862.

[45] Simonelli, M., Tuck, C., Aboulkhair, N. T., et al. “A Study on the Laser Spatter and the Oxidation Reactions During Selective Laser Melting of 316L Stainless Steel, Al-Si10-Mg, and Ti-6Al-4V,” *Metallurgical and Materials Transactions A*, V. 46, No. 9, 2015, pp. 3842–51.

[46] Beyhaghi, M., Rouhani, M., Hobley, J., et al. “*In-situ* and *ex-situ* comparison of oxidation of Inconel 718 manufactured by selective laser melting and conventional methods up to 650 °C,” *Applied Surface Science*, V. 569, 2021, p. 151037.

[47] Ohtsuki, T., and Pistorius, P. C. “Oxide Behavior During Laser Surface Melting,” *Metals*, V. 15, No. 6, 2025, p. 627.

[48] Bryndza, G., Tchuindjang, J. T., Chen, F., et al. “Review of the Microstructural Impact on Creep Mechanisms and Performance for Laser Powder Bed Fusion Inconel 718,” *Materials*, V. 18, No. 2, 2025, p. 276.

[49] Chaudhari, S. B., and Wakchaure, V. D. “A Comprehensive Review on the High-Temperature Behavior of Additively Manufactured Inconel 718.” International Conference on Additive Manufacturing. Springer, 2024. pp. 439–524.

[50] Markanday, J. F. S. “Applications of alloy design to cracking resistance of additively manufactured Ni-based alloys,” *Materials Science and Technology*, V. 38, No. 16, 2022, pp. 1300–14.

[51] Ghoussoub, J. N., Tang, Y. T., Dick-Cleland, W. J. B., et al. “On the Influence of Alloy Composition on the Additive Manufacturability of Ni-Based Superalloys,” *Metallurgical and Materials Transactions A*, V. 53, No. 3, 2022, pp. 962–83.

[52] Chen, Q., Zhao, Y., Strayer, S., et al. “Elucidating the effect of preheating temperature on melt pool morphology variation in Inconel 718 laser powder bed fusion via simulation and experiment,” *Additive Manufacturing*, V. 37, 2021, p. 101642.

[53] Pramod, S., and Kesavan, D. “Melting modes of laser powder bed fusion (L-PBF) processed IN718 alloy: Prediction and experimental analysis,” *Advances in Industrial and Manufacturing Engineering*, V. 6, 2023, p. 100106.

[54] Coen, V., Goossens, L., and Hooreweder, B. V. “Methodology and experimental validation of analytical melt pool models for laser powder bed fusion,” *Journal of Materials Processing Technology*, V. 304, 2022, p. 117547.

[55] Hasani, N., Dharmendra, C., Sanjari, M., et al. “Laser powder bed fused Inconel 718 in stress-relieved and solution heat-treated conditions,” *Materials Characterization*, V. 181, 2021, p. 111499.

[56] Jiang, R., Mostafaei, A., Wu, Z., et al. “Effect of heat treatment on microstructural evolution and hardness homogeneity in laser powder bed fusion of alloy 718,” *Additive Manufacturing*, V. 35, 2020, p. 101282.